Article

How to appropriately assess the oxygen reduction reaction activity of platinum group metal catalysts with rotating disk electrode

Yun-Fei Xia, Pan Guo, Jia-Zhan Li, Lei Zhao, Xu-Lei Sui, Yan Wang, Zhen-Bo Wang

wangzhb@hit.edu.cn (Z.-B.W.)
leizhao@hit.edu.cn (L.Z.)
suixulei@szu.edu.cn (X.-L.S.)

Highlights

Reference electrode usage specifications and mechanisms are illustrated

A 4-fold ORR activity discrepancy of Pt/C is found for different test protocols

An average adsorption model with self-consistent iterative algorithm is found

The coverage effects derived from the model can interpret the ORR hysteresis loop

Article

How to appropriately assess the oxygen reduction reaction activity of platinum group metal catalysts with rotating disk electrode

Yun-Fei Xia,[1,4,5] Pan Guo,[1,5] Jia-Zhan Li,[2] Lei Zhao,[1,*] Xu-Lei Sui,[3,*] Yan Wang,[4] and Zhen-Bo Wang[1,3,6,*]

SUMMARY

The sluggish oxygen reduction reaction (ORR) has becoming the bottleneck of largescale implementation of proton exchange membrane fuel cells. However, when it comes to the ORR activity assessing of platinum group metals (PGMs) with rotating disk electrode, the corresponding potential conversion vs. reversible hydrogen electrode, test protocols, and activity calculation processes are still in chaos in many published literatures. In this work, two standard calculation processes for PGM ORR activities are demonstrated, followed by a specification for the usage of reference electrodes. Then a 4-fold discrepancy in ORR activities obtained via different test protocols is found for the same Pt/C, and an average adsorption model and the "coverage effects" are proposed to illustrate the hysteresis loop between negative and positive-going ORR polarization plots. Finally, four motions over appropriate assessment of PGM ORR activity are emphasized, hoping to bring a fair communication platform for researchers from different groups.

INTRODUCTION

Proton exchange membrane fuel cells (PEMFCs) has been regarded as one of the most promising energy technologies to solve the energy crisis and environmental problems (He et al., 2020; Li et al., 2019; Liu et al., 2019; Ma et al., 2020; O'Hayre et al., 2016; Xiong et al., 2020). The last two decades witnesses the vigorous development of PEMFCs technology (Chen et al., 2019; Chong et al., 2018; Li et al., 2016; Paulus et al., 2002; Stamenkovic et al., 2007; Tian et al., 2019; Wang et al., 2013), and roadmaps have been scheduled by governments all over the world to grasp the potential industrial highland of the near future (European Commission, 2020; The Japan METI, 2018; The State Council of China, 2021; The US Department of Energy (DOE), 2016). But the sluggish oxygen reduction reaction (ORR), occurring in the cathode, limits the overall performance and efficiency of PEMFCs, and platinum group metals (PGMs) are the most widely used cathode catalysts as of today for they can achieve an acceptable activity and durability in the acidic and oxidative environments of cathode (Huang et al., 2021; Xu et al., 2020). While PEMFCs is still hindered from its largescale application due to the scarcity and high costs of PGMs (Dong et al., 2020a; Wang et al., 2020a). Great efforts have been paid on catalyst design (Chen et al., 2020a; Hu et al., 2020; Qin et al., 2020; Sandbeck et al., 2020; Zhang et al., 2020a), advanced characterization (Dong et al., 2020b; Wan et al., 2019; Wang et al., 2019c), simulation and theoretical studies (Chen et al., 2020c; Haile et al., 2020; Hammer and Nørskov, 2000; Liu et al., 2020a; Moriau et al., 2021; Nørskov et al., 2004) to get insight into the ORR mechanisms and reduce the Pt loading for PEMFCs. Those achievements, challenges, and prospects of PGMs for ORR during the last twenty years have been well summarized and analyzed by other researchers (Ma et al., 2020; Liu et al., 2020c; Ren et al., 2020; Wang et al., 2019a; Xie et al., 2020). However, when we looked up at those literatures, we found ambiguities in the thin-film rotating disk electrode (TF-RDE) tests (Figure 1) of ORR even in some works of top quality. The details of vital procedures, such as mass/specific activity calculation, potential conversion with respect to reversible hydrogen electrode (RHE) and protocol of ORR polarization tests, are not demonstrated in most published literatures, wherein unexpected variables may be unintentionally introduced, which may bring troubles to beginners and impede the development of PGM catalysts and PEMFCs *per se*.

In this work, two standard calculation processes of mass and specific activities are presented, followed by a brief introduction of hydrogen reference electrodes (HREs) and the formation mechanism of liquid junction

[1]MIIT Key Laboratory of Critical Materials Technology for New Energy Conversion and Storage, State Key Lab of Urban Water Resources and Environment, School of Chemistry and Chemical Engineering, Harbin Institute of Technology, Harbin 150001, China

[2]Department of Chemistry, Tsinghua University, Beijing 100084, China

[3]Shenzhen Key Laboratory of Special Functional Materials, College of Materials Science and Engineering, Shenzhen University, Shenzhen 518060, China

[4]School of Chemistry and Chemical Engineering, Harbin Institute of Technology, Harbin 150001, China

[5]These authors contributed equally

[6]Lead contact

*Correspondence:
wangzhb@hit.edu.cn
(Z.-B.W.),
leizhao@hit.edu.cn (L.Z.),
suixulei@szu.edu.cn (X.-L.S.)

https://doi.org/10.1016/j.isci.2021.103024
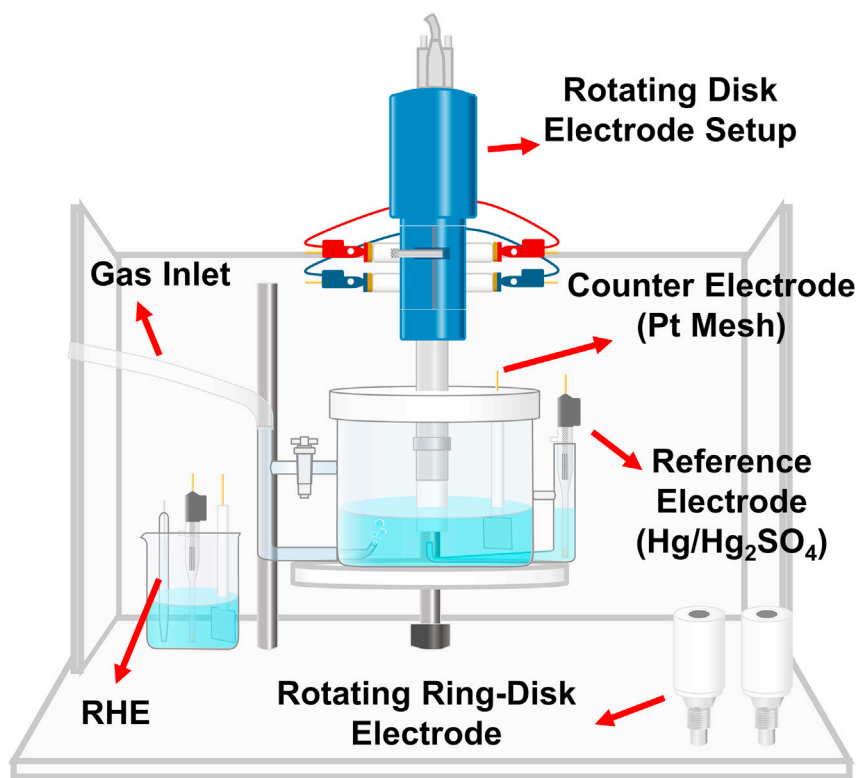
Figure 1. Sketch of typical rotating disk electrode setup (Pine Research, PHYCHEMi, US) for ORR tests

potential (E_j, originated from the interface of different electrolytes) (Brad and Faulkner, 2000) in practical test system. It should be highlighted even when the E_j term is considered, it will be inappropriate to calculate the potential differences between reference electrodes (REs) with any thermodynamic equation. And a 4-fold discrepancy in ORR activities obtained via different test protocols is found for the same Pt/C catalyst, then an average adsorption model based on minimum necessary assumptions and self-consistent iterative algorithm is established to demonstrate the coverage state of oxygen-containing species on PGM surface. The "coverage effects" derived from the model can interpret the formation mechanism of polarization hysteresis loop (the discrepancy between negative and positive-going ORR polarization plots from ~0.60 V to ~1.05 V) very well. At last, the standard potential conversion process, test protocols and activity calculation processes are emphasized to accurate evaluation of ORR performances of PGMs in TF-RDE tests, and the limitation of TF-RDE and its future development are also mentioned. More importantly, we also want to simplify and extend the average adsorption model in later works as an effective and general electrochemical approach to characterize the intrinsic ORR catalytic capabilities of PGMs for electro-catalysis society.

RESULTS

Mass and specific activities and their standard calculation processes

Mass activity (M_A), specific activity (S_A), and electrochemically active surface area (ECSA) are the fatal indicators describing the performance of PGM catalysts for ORR from different dimensions. M_A@0.9V (vs. RHE) is an ultimate activity indicator proposed by the US Department of energy (DOE target of 2025: 0.44 mA/μg_{Pt}) (The US Department of Energy (DOE), 2016). and a higher M_A means less Pt loading required for certain fuel cell system (<0.1 g_{Pt}/kW). ECSA is the exposed surface area of Pt per unit mass determined via hydrogen underpotential deposition (HUPD) or CO stripping (Chen et al., 2010; Vidal-Iglesias et al., 2012), and S_A@0.9V derived from M_A and ECSA represents the intrinsic activity of catalyst. By now TF-RDE (Figure 1) is the most widely used technique for fast *ex situ* screening of ORR catalysts because of its convenience and controllability (Chen et al., 2020b; Paulus et al., 2001; Shinozaki et al., 2015a, 2015b; Zhu et al., 2020), and typical test results are presented in Figure 2. Two standard pathways (current
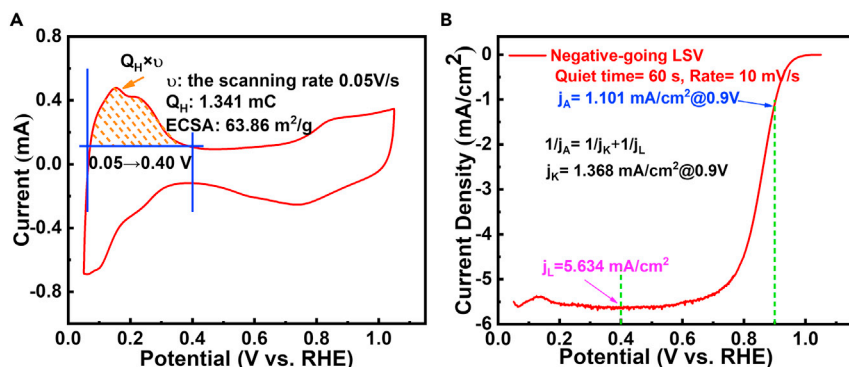
Figure 2. Tests of commercial 20% Pt/C (see characterizations in Figures S4 and S5) on TF-RDE in 0.1 M HClO$_4$ electrolyte

(A) Ar cyclic voltammetry (CV).

(B) ORR polarization tests; Pt loading 10 μg_{Pt}, Electrode area 0.2463 cm^2.

pathway: Equations 2.1 and 5.1; current density pathway: Equations 2.2 and 5.2) to calculating M$_A$/S$_A$ for PGMs are demonstrated as follows.

$$1/J_A = 1/J_K + 1/J_L \quad OR \quad 1/j_A = 1/j_K + 1/j_L, \quad Koutecky - Levich \ equation \qquad (Equation\ 1)$$
$$M_A = J_K/M_{Pt} \qquad (Equation\ 2.1)$$
$$M_A = j_K/m_{Pt} \qquad (Equation\ 2.2)$$
$$aECSA = Q_H/CD_{HUPD} \qquad (Equation\ 3)$$
$$ECSA = aECSA/M_{Pt} \qquad (Equation\ 4)$$
$$S_A = J_K/aECSA \qquad (Equation\ 5.1)$$
$$S_A = M_A/ECSA \neq j_K/ECSA \qquad (Equation\ 5.2)$$

J$_A$: the apparent current (mA), J$_K$: the kinetic current (mA), J$_L$: the limiting current (mA), j$_i$: the current densities (mA/cm^2); M$_A$: mA/μg_{Pt}, M$_{Pt}$: the absolute Pt loading (μg_{Pt}), m$_{Pt}$: the Pt loading density (μg_{Pt}/cm^2), aECSA: the absolute electrochemically active surface area (m$^2_{Pt}$), Q$_H$: the integral Faraday charge in hydrogen adsorption region (μC, Figure 2A and 0.05–0.40 V), CD$_{HUPD}$: the charge density of HUPD, ~210 μC/cm^2 for polycrystalline Pt (Chen et al., 2010), ECSA: m$^2_{Pt}$/g$_{Pt}$, S$_A$: mA/cm$^2_{Pt}$.

Simple though calculation processes are, caution should be exercised in the M$_A$ and S$_A$ calculations because issues could still be found in literatures published in recent years. The possible issues are summarized as follows: (1). The absence of K-L equation, which will lead to a smaller M$_A$ or S$_A$. (2). Arithmetic error originating from unit incoherence, for example, a typical ECSA value of 65 m$^2_{Pt}$/g$_{Pt}$ should converted to 0.65 cm$^2_{Pt}$/μg_{Pt} before calculation, and different mass activity units (1 mA/μg_{Pt} = 1 A/mg$_{Pt}$ = 1000 mA/mg$_{Pt}$) are misused by authors, which may cause errors of 1–3 orders of magnitude. (3). Unclear concepts about M$_A$ and S$_A$, for instance, incorrect formulas like M$_A$ = j$_K$/ECSA, M$_A$ = j$_K$/(m$_{Pt}$ ×ECSA), M$_A$ = j$_K$/M$_{Pt}$, S$_A$ = j$_K$/ECSA, and j$_K$ = lgj$_K$ are adopted. All these could give rise to the inaccuracy of catalyst activity, thus reducing the academic value of article and even making other researchers go astray.

More importantly, from Equation 5.2 (M$_A$ = S$_A$ ×ECSA), we can see the correlation between ECSA, S$_A$, and M$_A$ more explicitly. M$_A$ is a composite parameter that demonstrates the total apparent catalytic capability of Pt per unit mass, and then S$_A$ and ECSA together describe the details of M$_A$ from two different aspects. ECSA tells the exposed area of Pt per unit mass, and S$_A$ represents the intrinsic catalytic capability (turnover frequency, TOF (Paulus et al., 2002)) of Pt per unit exposed area. Figuratively speaking (Figure 3), a giraffe and an elephant (two different catalysts) may share the same weight (M$_A$), but the giraffe is taller (bigger ECSA) while the elephant is stronger (higher S$_A$). M$_A$ (0.44 mA/μg_{Pt}@0.9V) is the ultimate goal we pursue for the commercialization of PEMFCs, and ECSA and S$_A$ could tell us more details about how to achieve this target.

Hydrogen reference electrode and potential conversion vs. RHE

As shown in Figure 1, a typical TF-RDE setup usually involves three electrodes, i.e., working electrode (WE), counter electrode (CE) and RE. WE potentials obtained via various REs (like mercury-mercurous sulfate
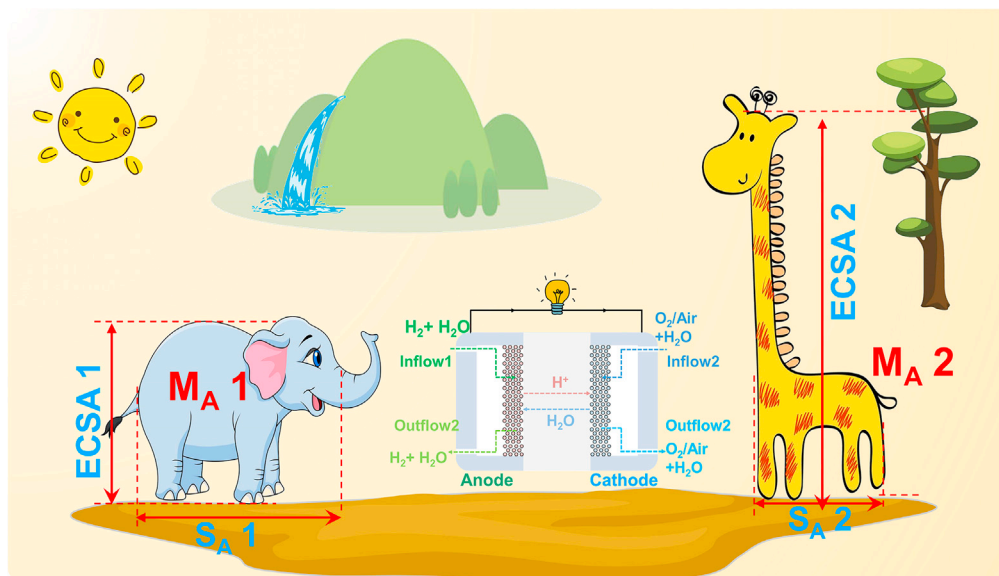
Figure 3. Schematic of the correlation between ECSA, S$_A$ and M$_A$

electrode [MSE] (Daudt et al., 2020; Shen et al., 2016), saturated calomel electrode (Fang et al., 2019; Liu et al., 2017), et al.) are usually converted to potentials of RHE scale (Jerkiewicz, 2020; Niu et al., 2020) for the convenience of comparison between different systems. The accuracy of potential conversion is of vital importance for ORR measurement of PGMs, especially with the amplification effect derived from K-L equation (Equation 1 and Table S3-1), (Brad and Faulkner, 2000; Paulus et al., 2001) which may finally lead to an error of an order of magnitude on ORR activity. However, the correlation between those electrodes, especially their potential conversion details in practical systems, is not illuminated in most literatures.

Brief history and correlation of HREs

Normal hydrogen electrode (NHE) is a thermodynamically imprecise device developed by researchers in early years for marking the baseline of electric potential, wherein platinum black, monobasic (1 N) strong acid of 1 mol/L, and bubbled H$_2$ of 1 atm are used for the realization of Reaction 1 (Figure 4A (Jerkiewicz, 2020)). While standard hydrogen electrode (SHE), an ideal model with absolute accuracy but cannot be physically attained, is late proposed as the zero point of potential, in which the H$^+$ activity (a_{H^+}) is 1 mol/L and the H$_2$ fugacity (f(H$_2$)) is 1 bar, and its potential is defined as 0 V at arbitrary temperature. One can treat NHE an approximate physical realization of SHE around room temperatures, where the effects of activity/fugacity coefficient and the vapor pressure of water are all neglected. Then RHE is a concept further developed from Equation 6.1, of which the activity and the fugacity of redox couple (H$^+$/H$_2$) are not necessarily in standard states. If we further fix the H$_2$ partial pressure around 1 bar, a simplified Equation 6.2 can be used to calculate the potential of RHE (WikiPedia, 2021; Brad and Faulkner, 2000; Jerkiewicz, 2020; Kamiya, 2013).

$$H^+\left(aq\right) + e^- \leftrightarrow \frac{1}{2}H_2(g) \quad \phi^0_{H^+/H_2} \overset{def}{=} 0 \text{ V} \qquad \text{(Reaction 1)}$$
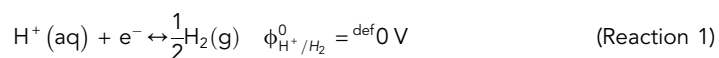
$$\phi_{RHE} = \phi^0_{H^+/H_2} + \frac{RT}{F}\ln\frac{a_{H^+}/a^0}{\sqrt{f(H_2)/p^0}} \qquad \text{(Equation 6.1)}$$

$$\phi_{RHE} = \phi^0_{H^+/H_2} + \frac{RT}{F}\ln a_{H^+}/a^0 = -59.2 \text{ mV} \times \text{pH} \qquad \text{(Equation 6.2)}$$

ϕ^0: the standard electrode potential (mV), ϕ_{RHE}: the RHE potential vs. SHE (mV), R: the general gas constant (8.314 J mol^{-1} K^{-1}), T: the absolute temperature (K), F: the Faraday constant (96,485 C/mol), a_i: the activity of i species (mol/L), a_0: the unit activity (1 mol/L), f(i): the fugacity of i gas (bar), p^0: the standard pressure (1 bar).
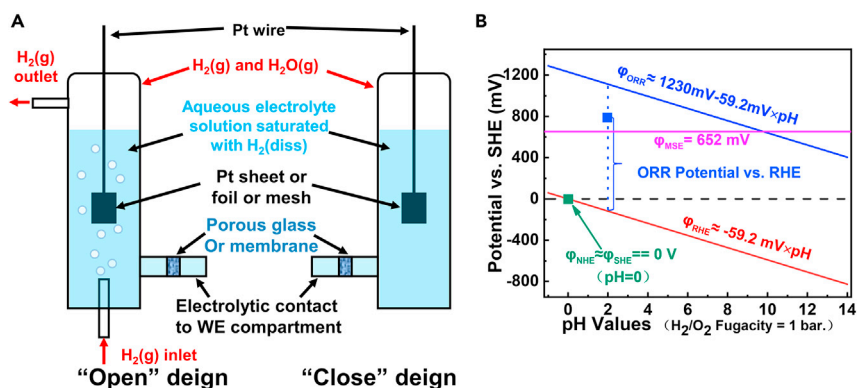
Figure 4. Hydrogen reference electrodes and the comparison between SHE, RHE, and MSE

(A) Hydrogen reference electrodes of "open" and "close" compartment design, Ref (Jerkiewicz, 2020), ACS, reproduced with permission.

(B) Relative potentials of RHE and MSE vs. SHE in electrolytes of different pH (MSE and ORR potentials see Figure S1).

Figure 4B demonstrates the thermodynamic correlation between different REs with SHE as the zero potential. The green solid point represents the potential of SHE (NHE), while the red solid line of a slope of −59.2 mV/pH and the horizontal magenta solid line in 652 mV stand for the potential of RHE and MSE as a function of pH, respectively. In addition, from Figure 4B we can see that ϕ_{RHE} and ϕ_{ORR} (all vs. SHE) share the same trend as a function of pH, indicating the effectiveness of comparison (like onset or half-wave potential (Brad and Faulkner, 2000)) between catalysts in electrolytes of different pH, and that is why RHE potential is adopted in the fields like ORR, oxygen evolution reaction (OER), hydrogen evolution reaction, CO_2 reduction reaction, nitrogen reduction reaction, and lead acid batteries (Carpente et al., 1996; Jiang et al., 2016; Yan et al., 2019; Zhang et al., 2020b; Zhao et al., 2019).

Calibration of electrode potential with RHE in practical electrolyte

When it comes to the potential conversion of MSE from SHE to RHE in practical system, intuitively, derived from Equations 6 and S1, its mathematical expression could be written as Equation 7 (Wang et al., 2019b).

$$\phi_{MSE-RHE} = \phi_{MSE} + 59.2 \text{ mV} \times pH \qquad \text{(Equation 7)}$$
$$\phi_{MSE-RHE} = \phi_{MSE} + 59.2 \text{ mV} \times pH + E_j \qquad \text{(Equation 8)}$$

$\phi_{MSE-RHE}$: the MSE potential vs. RHE in certain electrolyte (mV), ϕ_{MSE}: the MSE potential vs. SHE (652 mV), E_j: mV.

However, Equation 7 is thermodynamically right but can only be used for potential calibration when most of E_j could be eliminated (such as the introduction of double salt bridge REs) (Brad and Faulkner, 2000; Carpente et al., 1996; Jerkiewicz, 2020; Niu et al., 2020). A typical test device (Figure 5A) can be used to shed light on the potential conversion issues in practical aqueous solutions. An MSE (652 mV vs. NHE/SHE) is calibrated in 1.0 M $HClO_4$ aqueous solution with a homemade RHE (experimental details in STAR Methods) acting as the RE. Due to the existence of E_j (Figure 5B, the detailed formation mechanism in Figure S2), E_j term should be introduced in the potential conversion equation, as demonstrated in Figure 5C and Equation 8.

Figure 5D demonstrates the discrepancy between thermodynamic values with and without the consideration of E_j (see details in Table S2). The red solid line ($\phi_{Ther-RHE}$) is calculated with Equation 7 and the blue line ($\phi_{Ther+Ej-RHE}$) is derived from Equation 8, while the orange line ($\phi_{Exp-RHE}$) is obtained from the experimental data of MSE calibrated with RHE. A good fitting between thermodynamic and experimental values is achieved after corrections of pH and E_j terms, confirming the effectiveness of introductions of E_j and Henderson equation (Equation S3). However, it does not mean that Equation 8 could be used for potential conversions in practical test systems because REs can't be stable throughout their service lives (Niu et al., 2020). The potential of stale MSE vs. RHE ($\phi_{Stale-RHE}$) is also calibrated in the same way (green line in Figure 5D), and its deviation from the experimental values of an all-new MSE (blue line) may be attributed to the evolution of chemical compositions inside MSE (like the photocatalytic decomposition of Hg_2SO_4),
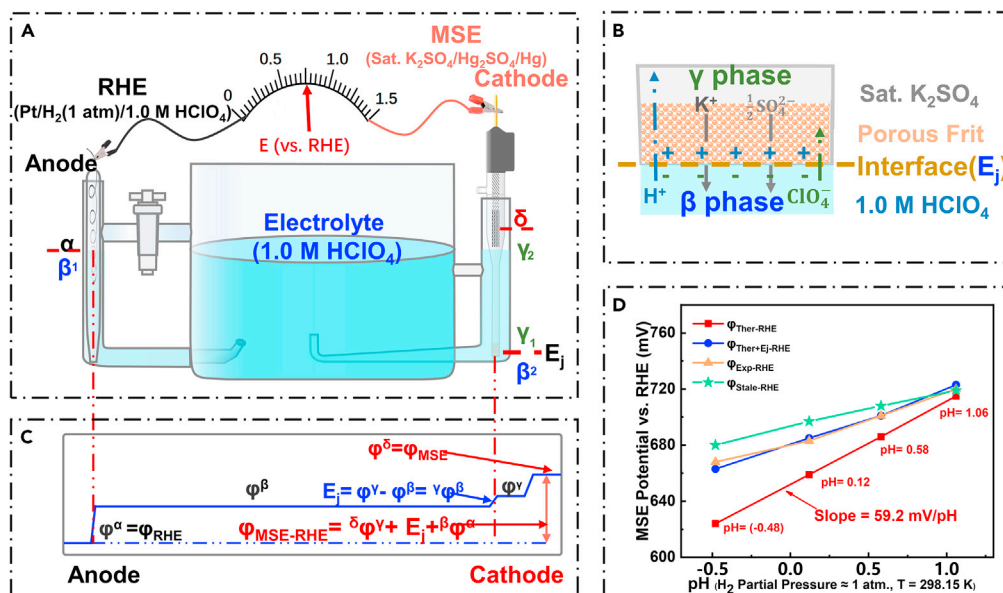
Figure 5. Calibration of MSE with RHE in HClO$_4$ electrolytes

(A) A typical test device.

(B) Schematic of the formation mechanism of E$_j$.

(C) Simplified potential profile in test device.

(D) Calibration of MSE with RHE in electrolytes of different pH.

(National Center for Biotechnology Information, 2021) meaning MSE should be calibrated with RHE periodically to ensure its reliability.

From the above facts, we can conclude that it will be inappropriate to calculate the potentials of REs or redoxes in WEs vs. RHE with any thermodynamic equations, because E$_j$ and compositional evolutions inside REs can both give rise to unexpected influences to final results. Therefore, we strongly recommend that: (1). RHE with the same electrolyte as bulk solution, whereby E$_j$ will not exist and there is no need to consider the activity coefficient of H$^+$, should be used as RE directly for ORR or other electro-catalyzes (Gong et al., 2019; Kong et al., 2020; Liu et al., 2020b); or (2). Calibrate other REs with RHEs in the test electrolytes just before the tests are performed (Tian et al., 2019; Wang et al., 2018). Only in this way can the impacts derived from E$_j$ and any other uncontrolled aspects from REs *per se* could be alleviated.

Effects of test protocol on the ORR performance of PGMs

Linear sweep voltammetry (LSV) and staircase voltammetry (SCV) in O$_2$ saturated electrolytes are usually performed on TF-RDE to estimate the ORR catalytic capabilities of PGM-based catalysts, however their subtle distinctions and specific test details are rarely discussed (Ban et al., 2016; Montella, 2017; Paulus et al., 2001; Shinozaki et al., 2015b; Wan et al., 2015). From the potential profiles of LSV and SCV (see also Figure S3), we could know that SCV is a quasi-steady process, wherein the non-faradic current derived from the charging of double-layer could be neglected. While LSV is a semi-steady process, and its capacitive current from double-layer charging (Figure 6A, gained from corrected Ar LSV, and see Figure S7 for details) should be subtracted from its O$_2$ LSV under the same test condition (Brad and Faulkner, 2000). Figure 6B shows the comparison between negative-going original LSV, background-corrected LSV and SCV for commercial Pt/C, and the result shows no obvious difference between negative-going background-corrected LSV and SCV.

Positive-going LSV and SCV, which are also considerably adopted by many researchers for ORR tests, were also performed and the results are presented in Figure 6C. The polarization hysteresis loops are found for both LSV and SCV, especially the ORR M$_A$ obtained via positive-going LSV reaches 0.137 mA/ug$_{Pt}$, which is 4 times higher than its negative-going counterpart (see details in Table S3-1), and these phenomena are also reported by other researchers (Shinozaki et al., 2015b; Wan et al., 2015). The cathodic current density
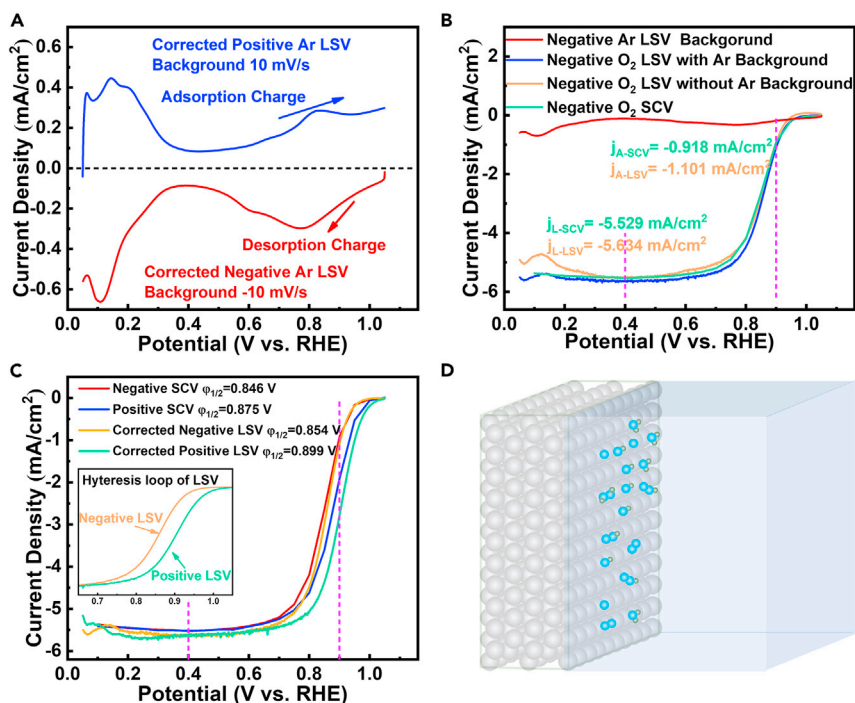
Figure 6. Effects of test protocol on the ORR performance of commercial Pt/C
(A) Corrected Ar LSVs.
(B) Comparison between negative-going LSV and SCV.
(C) LSV and SCV polarization plots with different scanning directions.
(D) Schematic of adsorption of oxygen-containing spectators on Pt surface in $HClO_4$ (0.40–1.05 V).

can be written as Equation 9 (Paulus et al., 2002; Stamenkovic et al., 2007). As all these tests are obtained from one RDE of the same Pt/C, the catalyst *per se*, the exposed crystalline facets, the applied overpotential, and the mass transport conditions are exactly the same (parameters like k, C_{O_2}, a, E, β, and γ in Equation 9 are the same for all tests); thus the discrepancy of ORR polarization plots for negative and positive-going LSVs/SCVs should be attributed to their different coverage degrees (θ_{ad}) of oxygen-containing species spectators (Figure 6D) on Pt surface (Chen et al., 2020c; Liu et al., 2020c; Paulus et al., 2002; Stamenkovic et al., 2007), as implied by the asymmetric adsorption/desorption currents (from 0.40 V to 1.05 V) in Figure 6A.

$$j_c = nekC_{O_2}(1 - \theta_{ad})^a \exp\left(\frac{-\beta FE}{RT}\right)\exp\left(\frac{-\gamma r\theta_{ad}}{RT}\right)\Big/ S_G \qquad \text{(Equation 9)}$$

j_C: the cathodic current density (mA/cm^2), n: the number of electrons (here is 4), e: the elementary charge (1.60 × 10^{-19} C), k: the rate constant under unit reactants ((mol·L^{-1})$^{-1}$·s^{-1}), C_{O_2}: the concentration of O_2 (mol/L), θ_{ad}: the absolute coverage degree, a: a constant coefficient, E: the applied potential (V), β and γ: the symmetry factors, $r\theta_{ad}$: the effects of coverage on the adsorption of adsorbates, S_G: the geometric area of electrode (cm^2).

To further quantify the coverage effects on the formation of hysteresis loop for negative/positive-going LSVs, an average adsorption model, wherein the species diversity of oxygen-containing spectators adsorbing on Pt surface is ignored, is proposed to calculate the relative coverages (θ', not the real coverage degree θ_{ad}, and see definition in Equation S9) of oxygen-containing adsorbates on Pt. It is reasonable to assume the adsorption of negative-going Ar/O_2 LSVs before tests are in equilibrium because they were held at 1.05 V (the open-circuit potential [OCP] of the commercial 20% Pt/C) for 60 s, and the negative-going Ar LSV (O_2 LSV is too complex) is selected to establish the average adsorption model and demonstrate the adsorption situation of Pt/C between 0.40 and 1.05 V. The basic hypotheses are as follows:
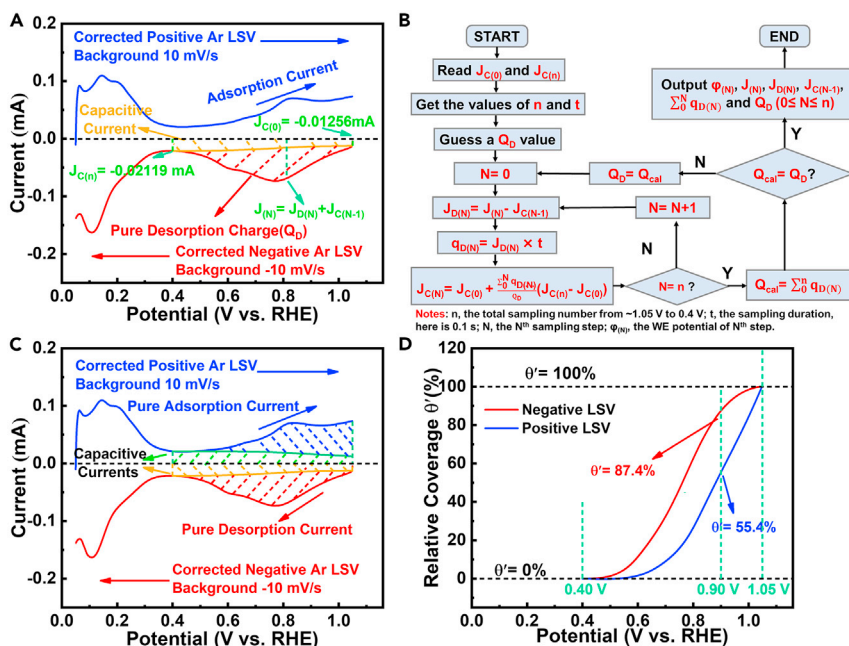
Figure 7. Establishment of average adsorption model

(A) Basic hypotheses.

(B) Self-consistent iterative algorithm to extract pure desorption current from its total current.

(C) Extraction of pure desorption/adsorption currents from Ar LSVs.

(D) Relative coverages (θ') on Pt/C with different scanning directions (0.40–1.05 V).

(1) The adsorption state on Pt surface in Ar LSVs are close to those in O_2 LSVs, for the adsorption of oxygen-containing spectators is relatively strong (Nørskov et al., 2004; Viswanathan et al., 2012) and thus will not be affected noticeably by ORR; (2) θ' at 1.05 V ($\theta'_{(0)}$) and 0.40 V ($\theta'_{(n)}$) are defined to be 100% and 0%, respectively; (3) The total negative current ($J_{(N)}$, see Figures 7A and 7B) consists of double-layer charging current ($J_{C(N-1)}$) and desorption current ($J_{D(N)}$), namely, $J_{(N)} = J_{D(N)} + J_{C(N-1)}$; (4) The initial oxygen desorption process at $\sim$1.05 V is slow enough, the initial current pulse around which only corresponds to $J_{C(0)}$, i.e., $J_{(0)} = J_{C(0)}$; (5) There only exists $J_{C(n)}$ at 0.40 V (Brad and Faulkner, 2000) viz,., $J_{(n)} = J_{C(n)}$; (6) The adsorption from 0.40 to 1.05 V is monolayer adsorption and the adsorbate diversity on Pt surface is neglected and averaged (Conway, 1995; Samet et al., 2008), meaning θ' is a linear function of integrated desorption charge ($\theta'_{(N)} \overset{\text{def}}{=} (Q_D - \sum_0^N q_{D(N)})/Q_D$) and J_C is a linear function of θ' $\left(J_{C(N)} = J_{C(0)} + \left(1 - \theta'_{(N)}\right)\left(J_{C(n)} - J_{C(0)}\right) \right)$, see details in Figure S10 and Equations S4–S10).

The details of calculation process and its corresponding calculated results are shown in Figures 7B and 7C and Table S5, then the final θ'-potential plots (Figure 7D) is obtained from the pure desorption/adsorption current integrations between 1.05 and 0.40 V in Figure 7C. A sluggish desorption process around 1.05 V and the same hysteresis loop resembling Figure 6C are observed, corroborating the rationality and effectiveness of our model. In addition, from Figure 7D, we could find that the negative-going Ar LSV is accompanied with a sluggish oxygen-containing spectator desorption in high potential regime (>0.9 V) and thus leads to a higher θ' (87.4%) at 0.9 V; while the positive-going Ar LSV is benefited from the sluggish adsorption in low potential regime (<0.9 V) and brings a lower θ' (55.4%), which finally result in the emersion of hysteresis loop between LSVs/SCVs of different scanning directions (Figure 6C and Equation 9).

The effects of scanning potential window and rate (Figures S11–S14), the selection of j_L (Figure S15), and the iR-drop correction issues (Figures S16 and S17) are also discussed in supplemental information. Based on the above analyses, we could know that test protocol could have a tremendous impact on PGMs polarization tests. The "coverage effects" along with the amplification effect of K–L equation (Equation 1 and Table S3-1) may lead to a 4-fold discrepancy in ORR activities obtained via different test protocols for the same

PGM catalyst (PGM-free catalysts like Fe–N–C will not be affected, see discussions in Figures S6 and S9). However, the details of test protocols are rarely mentioned in most published works, which may bring a bit of hassle for the fair comparison between test results from different groups. Since the "coverage effects" also exists in membrane electrode assembly (MEA) in operating conditions and to simulate the standard MEA polarization protocol proposed by DOE (Table S4 (The US Department of Energy (DOE), 2016)), it is highly recommended to adopt reciprocating LSV/SCV (from OCP to 0.05 V, then from 0.05 V back to OCP, as shown in Figure 6C and Table S3-1) to assess the activities of PGMs.

DISCUSSION

PEMFCs is of crucial importance to realize the carbon-neutral society for the sustainable development of human kind (Asset and Atanassov, 2020), and enormous advances have been achieved on mechanism study, catalyst synthesis/characterization, MEA simulation/fabrication, and even preliminary commercialization of electric vehicles during the last decade (Deng et al., 2020; E4tech, 2018; Wang et al., 2020b). PGM-based catalysts are still indispensable for the foreseeable largescale application of PEMFCs, nevertheless some fundamental issues concerning potential conversion and activity/durability tests still need to be clarified and standardized for the better development of pivotal ORR catalysts. The following proposals are urgently to be motivated: (1) RHE should be used as RE as far as possible, and if other REs are adopted, their details of potential conversion vs. RHE should be illustrated, and there is no need to conduct iR-drop correction if Luggin capillary is placed correctly in TF-RDE test; (2) To simulate the standard MEA polarization protocol proposed by DOE and narrow the gap of ORR activities obtained via TF-RDE and MEA, reciprocating LSV/SCV should be performed to characterize the ORR performances of PGMs; (3) Connotations like M_A and S_A should be defined precisely, and K-L equation as well as the selection of j_L should be emphasized; (4) The details of calculation processes, such as m_{Pt}, j_A, j_L, and ECSA et al., should be listed in article or supplemental information for the better readability for readers. Furthermore, considering the limited mass transport in TF-RDE and its discrepancy in test conditions with respect to MEA, whose fabrication process is very much an art, floating electrode (Lin et al., 2020; Zalitis et al., 2013) and gas diffusion electrode (Inaba et al., 2018; Mardle et al., 2020; Roudbari et al., 2020) techniques have been proposed in recent years and are under rapid development to bridge the activity gap between TF-RDE and MEA while maintaining its simplicity, convenience, and controllability.

Limitations of the study

In this work, we have emphasized the considerations concerning the appropriate evaluation of PGM ORR catalysts, and 4 motions are proposed hoping to bring a fair communication platform for researchers from different groups. However, those experiments were all conducted on TF-RDE instrument, a general equipment widely taken by researchers for the fast *ex situ* screening of ORR catalysts but whose environments are different from those in an operating MEA. More efforts and investigations should be done via MEA tests for PGM or PGM-free ORR catalysts, and our laboratory is constructing the MEA test platform right now.

STAR★METHODS

Detailed methods are provided in the online version of this paper and include the following:

- KEY RESOURCES TABLE
- RESOURCE AVAILABILITY
  - Lead contact
  - Materials availability
  - Data and code availability
- METHOD DETAILS
  - Preparation of reversible hydrogen electrode (RHE)
  - Calibration of REs with respect to RHE
  - Synthesis of Fe-N-C PGM-free catalyst
  - Material characterization
  - The preparation of working electrode (WE)
  - The Linear sweep voltammetry (LSV) for ORR
  - The staircase voltammetry (SCV) for ORR
  - The hydrogen peroxide yield (H_2O_2%) calculation

AUTHOR CONTRIBUTIONS

Conceptualization, Y.-F. X., P. G., L. Z., X.-L. S., and Z.-B. W.; methodology, Y.-F. X., J.-Z. L., L. Z., X.-L. S., and Z.-B. W.; validation, P. G., J.-Z. L., L. Z., and X.-L. S.; investigation, Y.-F. X. and P. G.; resources, L. Z., X.-L. S., Y. W., and Z.-B. W.; writing-original draft, Y.-F. X.; writing-review & editing, Y.-F. X., J.-Z. L., L. Z., X.-L. S., Y. W., and Z.-B. W.; visualization, Y.-F. X.; supervision and funding acquisition, L. Z., X.-L. S., and Z.-B. W.; project administration, Z.-B. W. All authors reviewed, revised, and approved of this manuscript.

DECLARATION OF INTERESTS

The authors declare no competing interests.

REFERENCES

Asset, T., and Atanassov, P. (2020). Iron-nitrogen-carbon catalysts for proton exchange membrane fuel cells. Joule 4, 33–44. https://doi.org/10.1016/j.joule.2019.12.002.

Ban, Z., Kätelhön, E., and Compton, R.G. (2016). Voltammetry of porous layers: staircase vs analog voltammetry. J. Electroanal. Chem. 776, 25–33. https://doi.org/10.1016/j.jelechem.2016.06.003.

Brad, A.J., and Faulkner, L.R. (2000). Electrochemical Methods: Fundamentals and Applications (John Wiley & Sons, Inc.).

Carpente, M.K., Bernardi, D.M., and Wertz, J.A. (1996). The use of Hg/Hg$_2$SO$_4$ reference electrodes in valve-regulated lead/acid cells. J. Power Sourc. 63, 15–22. https://doi.org/10.1016/S0378-7753(96)02436-6.

Chen, L., Liu, X., Zheng, L., Li, Y., Guo, X., Wan, X., Liu, Q., Shang, J., and Shui, J. (2019). Insights into the role of active site density in the fuel cell performance of Co–N–C catalysts. Appl. Catal. B Environ. 256, 117849–117856. https://doi.org/10.1016/j.apcatb.2019.117849.

Chen, Q.S., Solla-Gullón, J., Sun, S.G., and Feliu, J.M. (2010). The potential of zero total charge of Pt nanoparticles and polycrystalline electrodes with different surface structure: the role of anion adsorption in fundamental electrocatalysis. Electrochim. Acta 55, 7982–7994. https://doi.org/10.1016/j.electacta.2010.03.050.

Chen, S., Li, M., Gao, M., Jin, J., van Spronsen, M.A., Salmeron, M.B., and Yang, P. (2020a). High-performance Pt–Co nanoframes for fuel-cell electrocatalysis. Nano Lett. 20, 1974–1979. https://doi.org/10.1021/acs.nanolett.9b05251.

Chen, W., Xiang, Q., Peng, T., Song, C., Shang, W., Deng, T., and Wu, J. (2020b). Reconsidering the benchmarking evaluation of catalytic activity in oxygen reduction reaction. iScience 23, 101532. https://doi.org/10.1016/j.isci.2020.101532.

Chen, Y., Cheng, T., and Goddard, W.A., Iii (2020c). Atomistic explanation of the dramatically improved oxygen reduction reaction of jagged platinum nanowires, 50 times better than Pt. J. Am. Chem. Soc. 142, 8625–8632. https://doi.org/10.1021/jacs.9b13218.

Chong, L.N., Wen, J.G., Kubal, J., Sen, F.G., Zou, J.X., Greeley, J., Chan, M., Barkholtz, H., Ding, W.J., and Liu, D.J. (2018). Ultralow-loading platinum–cobalt fuel cell catalysts derived from imidazolate frameworks. Science 362, 1276–1281. https://doi.org/10.1126/science.aau0630.

Conway, B.E. (1995). Electrochemical oxide film formation at noble metals as a surface-chemical process. Prog. Surf. Sci. 49, 331–452. https://doi.org/10.1016/0079-6816(95)00040-6.

Daudt, N.F., Poozhikunnath, A., Yu, H., Bonville, L., and Maric, R. (2020). Nano-sized Pt–NbO$_x$ supported on TiN as cost-effective electrocatalyst for oxygen reduction reaction. Mater. Renew. Sustain. Energy 9, 18–34. https://doi.org/10.1007/s40243-020-00179-1.

Deng, X., Zhang, J., Fan, Z., Tan, W., Yang, G., Wang, W., Zhou, W., and Shao, Z. (2020). Understanding and engineering of multiphase transport processes in membrane electrode assembly of proton-exchange membrane fuel cells with a focus on the cathode catalyst layer: a review. Energy Fuels 34, 9175–9188. https://doi.org/10.1021/acs.energyfuels.0c02101.

Dong, C., Li, Y., Cheng, D., Zhang, M., Liu, J., Wang, Y.-G., Xiao, D., and Ma, D. (2020a). Supported metal clusters: fabrication and application in heterogeneous catalysis. ACS Catal. 10, 11011–11045. https://doi.org/10.1021/acscatal.0c02818.

Dong, J.C., Su, M., Briega-Martos, V., Li, L., Le, J.B., Radjenovic, P., Zhou, X.S., Feliu, J.M., Tian, Z.Q., and Li, J.F. (2020b). Direct in situ Raman spectroscopic evidence of oxygen reduction reaction intermediates at high-index Pt(hkl) surfaces. J. Am. Chem. Soc. 142, 715–719. https://doi.org/10.1021/jacs.9b12803.

E4tech. (2018). The Fuel Cell Industry Review 2018 (E4tech).

European Commission (2020). Powering a Climate-Neutral Economy: Commission Sets Out Plans for the Energy System of the Future and Clean Hydrogen. https://ec.europa.eu/commission/presscorner/detail/en/ip_20_1259.

Fang, D.H., Wan, L., Jiang, Q.K., Zhang, H.J., Tang, X.J., Qin, X.P., Shao, Z.G., and Wei, Z.D. (2019). Wavy PtCu alloy nanowire networks with abundant surface defects enhanced oxygen reduction reaction. Nano Res. 12, 2766–2773. https://doi.org/10.1007/s12274-019-2511-8.

Gong, M.X., Deng, Z.P., Xiao, D.D., Han, L.L., Zhao, T.H., Lu, Y., Shen, T., Liu, X.P., Lin, R.Q., Huang, T., et al. (2019). One-nanometer-thick Pt$_3$Ni bimetallic alloy nanowires advanced oxygen reduction reaction: integrating multiple advantages into one catalyst. ACS Catal. 9, 4488–4494. https://doi.org/10.1021/acscatal.9b00603.

Haile, A.S., Yohannes, W., and Mekonnen, Y.S. (2020). Oxygen reduction reaction on Pt-skin Pt$_3$V(111) fuel cell cathode: a density functional

theory study. RSC Adv. *10*, 27346–27356. https://doi.org/10.1039/d0ra02972f.

Hammer, B., and Nørskov, J.K. (2000). Theoretical surface science and catalysis - calculations and concepts. In Advances in Catalysis, Vol 45: Impact of Surface Science on Catalysis, B.C. Gates and H. Knozinger, eds., pp. 71–129. https://doi.org/10.1016/S0360-0564(02)45013-4.

He, Y.H., Liu, S.W., Priest, C., Shi, Q.R., and Wu, G. (2020). Atomically dispersed metal-nitrogen-carbon catalysts for fuel cells: advances in catalyst design, electrode performance, and durability improvement. Chem. Soc. Rev. *49*, 3484–3524. https://doi.org/10.1039/c9cs00903e.

Hu, Y., Jensen, J.O., Cleemann, L.N., Brandes, B.A., and Li, Q. (2020). Synthesis of Pt-rare earth metal nanoalloys. J. Am. Chem. Soc. *142*, 953–961. https://doi.org/10.1021/jacs.9b10813.

Huang, L., Zaman, S., Tian, X., Wang, Z., Fang, W., and Xia, B.Y. (2021). Advanced platinum-based oxygen reduction electrocatalysts for fuel cells. Acc. Chem. Res. *54*, 311–322. https://doi.org/10.1021/acs.accounts.0c00488.

Inaba, M., Jensen, A.W., Sievers, G.W., Escudero-Escribano, M., Zana, A., and Arenz, M. (2018). Benchmarking high surface area electrocatalysts in a gas diffusion electrode: measurement of oxygen reduction activities under realistic conditions. Energy Environ. Sci. *11*, 988–994. https://doi.org/10.1039/c8ee00019k.

Jerkiewicz, G. (2020). Standard and reversible hydrogen electrodes: theory, design, operation, and applications. ACS Catal. *10*, 8409–8417. https://doi.org/10.1021/acscatal.0c02046.

Jiang, W.J., Gu, L., Li, L., Zhang, Y., Zhang, X., Zhang, L.J., Wang, J.Q., Hu, J.S., Wei, Z.D., and Wan, L.J. (2016). Understanding the high activity of Fe–N–C electrocatalysts in oxygen reduction: Fe/Fe$_3$C nanoparticles boost the activity of Fe–N$_x$. J. Am. Chem. Soc. *138*, 3570–3578. https://doi.org/10.1021/jacs.6b00757.

Kamiya, N. (2013). Development of an electrolysis-reversible hydrogen electrode (E-RHE). ECS Trans. *50*, 25–31. https://doi.org/10.1149/05019.0025ecst.

Kong, Z.J., Maswadeh, Y., Vargas, J.A., Shan, S.Y., Wu, Z.P., Kareem, H., Leff, A.C., Tran, D.T., Chang, F.F., Yan, S., et al. (2020). Origin of high activity and durability of twisty nanowire alloy catalysts under oxygen reduction and fuel cell operating conditions. J. Am. Chem. Soc. *142*, 1287–1299. https://doi.org/10.1021/jacs.9b10239.

Li, J.Z., Zhang, H.G., Samarakoon, W., Shan, W.T., Cullen, D.A., Karakalos, S., Chen, M.J., Gu, D.M., More, K.L., Wang, G.F., et al. (2019). Thermally driven structure and performance evolution of atomically dispersed FeN$_4$ sites for oxygen reduction. Angew. Chem. Int. Ed. *58*, 18971–18980. https://doi.org/10.1002/anie.201909312.

Li, M.F., Zhao, Z.P., Cheng, T., Fortunelli, A., Chen, C.Y., Yu, R., Zhang, Q.H., Gu, L., Merinov, B.V., Lin, Z.Y., et al. (2016). Ultrafine jagged platinum nanowires enable ultrahigh mass activity for the oxygen reduction reaction. Science *354*, 1414–1419. https://doi.org/10.1126/science.aaf9050.

Lin, X., Zalitis, C.M., Sharman, J., and Kucernak, A. (2020). Electrocatalyst performance at the gas/electrolyte interface under high-mass-transport conditions: optimization of the "floating electrode" method. ACS Appl. Mater. Inter. *12*, 47467–47481. https://doi.org/10.1021/acsami.0c12718.

Liu, J., Jiao, M.G., Lu, L.L., Barkholtz, H.M., Li, Y.P., Wang, Y., Jiang, L.H., Wu, Z.J., Liu, D.J., Zhuang, L., et al. (2017). High performance platinum single atom electrocatalyst for oxygen reduction reaction. Nat. Commun. *8*, 15938–15947. https://doi.org/10.1038/ncomms15938.

Liu, M., Zhao, Z., Duan, X., and Huang, Y. (2019). Nanoscale structure design for high-performance Pt-based ORR catalysts. Adv. Mater. *31*, 1802234–1802241. https://doi.org/10.1002/adma.201802234.

Liu, Q., Li, Y., Zheng, L., Shang, J., Liu, X., Yu, R., and Shui, J. (2020a). Sequential synthesis and active-site coordination principle of precious metal single-atom catalysts for oxygen reduction reaction and PEM fuel cells. Adv. Energy Mater. *10*, 2000689–2000696. https://doi.org/10.1002/aenm.202000689.

Liu, Z.K., Yin, Y.H., Yang, D.J., Zhang, C.M., Ming, P.W., Li, B., and Yang, S.T. (2020b). Efficient synthesis of Pt–Co nanowires as cathode catalysts for proton exchange membrane fuel cells. RSC Adv. *10*, 6287–6296. https://doi.org/10.1039/d0ra00264j.

Liu, Z.Y., Zhao, Z.P., Peng, B.S., Duan, X.F., and Huang, Y. (2020c). Beyond extended surfaces: understanding the oxygen reduction reaction on nanocatalysts. J. Am. Chem. Soc. *142*, 17812–17827. https://doi.org/10.1021/jacs.0c07696.

Ma, Z., Cano, Z.P., Yu, A.P., Chen, Z.W., Jiang, G.P., Fu, X.G., Yang, L., Wu, T.P., Bai, Z.Y., and Lu, J. (2020). Enhancing oxygen reduction activity of Pt-based electrocatalysts: from theoretical mechanisms to practical methods. Angew. Chem. Int. Ed. *59*, 18334–18348. https://doi.org/10.1002/anie.202003654.

Mardle, P., Thirunavukkarasu, G., Guan, S., Chiu, Y.-L., and Du, S. (2020). Comparative study of PtNi nanowire array electrodes toward oxygen reduction reaction by half-cell measurement and PEMFC test. ACS Appl. Mater. Inter. *12*, 42832–42841. https://doi.org/10.1021/acsami.0c11531.

Montella, C. (2017). Further investigation of the equivalence of staircase and linear scan voltammograms. I- Sampling conditions for reversible reactions involving soluble species. J. Electroanal. Chem. *796*, 96–107. https://doi.org/10.1016/j.jelechem.2017.04.048.

Moriau, L.J., Hrnjić, A., Pavlišič, A., Kamšek, A.R., Petek, U., Ruiz-Zepeda, F., Šala, M., Pavko, L., Šelih, V.S., Bele, M., et al. (2021). Resolving the nanoparticles' structure–property relationships at the atomic level: a study of Pt-based electrocatalysts. iScience *24*, 102102. https://doi.org/10.1016/j.isci.2021.102102.

National Center for Biotechnology Information (2021). PubChem Annotation Record for MERCUROUS SULFATE, Source: Hazardous Substances Data Bank (HSDB), Retrieved August 7, 2021 from https://pubchem.ncbi.nlm.nih.gov/source/hsdb/1206#section=Density.

Niu, S., Li, S., Du, Y., Han, X., and Xu, P. (2020). How to reliably report the overpotential of an electrocatalyst. ACS Energy Lett. *5*, 1083–1087. https://doi.org/10.1021/acsenergylett.0c00321.

Nørskov, J.K., Rossmeisl, J., Logadottir, A., and Lindqvist, L. (2004). Origin of the overpotential for oxygen reduction at a fuel-cell cathode. J. Phys. Chem. B *108*, 17886–17892. https://doi.org/10.1021/jp047349j.

O'Hayre, R., Cha, S.W., Colella, W.G., and Prinz, F.B. (2016). Fuel Cell Fundamentals, 3rd Edition (John Wiley & Sons, Inc.). https://doi.org/10.1002/9781119191766.

Paulus, U.A., Schmidt, T.J., Gasteiger, H.A., and Behm, R.J. (2001). Oxygen reduction on a high-surface area Pt/Vulcan carbon catalyst: a thin-film rotating ring-disk electrode study. J. Electroanal. Chem. *495*, 134–145. https://doi.org/10.1016/s0022-0728(00)00407-1.

Paulus, U.A., Wokaun, A., Scherer, G.G., Schmidt, T.J., Stamenkovic, V., Radmilovic, V., Markovic, N.M., and Ross, P.N. (2002). Oxygen reduction on carbon-supported Pt–Ni and Pt–Co alloy catalysts. J. Phys. Chem. B *106*, 4181–4191. https://doi.org/10.1021/jp013442l.

Qin, Y., Zhang, W., Guo, K., Liu, X., Liu, J., Liang, X., Wang, X., Gao, D., Gan, L., Zhu, Y., et al. (2020). Fine-tuning intrinsic strain in penta-twinned Pt–Cu–Mn nanoframes boosts oxygen reduction catalysis. Adv. Funct. Mater. *30*, 1910107–1910114. https://doi.org/10.1002/adfm.201910107.

Ren, X., Lv, Q., Liu, L., Liu, B., Wang, Y., Liu, A., and Wu, G. (2020). Current progress of Pt and Pt-based electrocatalysts used for fuel cells. Sustain. Energy Fuels *4*, 15–30. https://doi.org/10.1039/c9se00460b.

Roudbari, M.N., Ojani, R., and Raoof, J.B. (2020). Nitrogen functionalized carbon nanotubes as a support of platinum electrocatalysts for performance improvement of ORR using fuel cell cathodic half-cell. Renew. Energy *159*, 1015–1028. https://doi.org/10.1016/j.renene.2020.06.028.

Samet, Y., Mefteh, R., Abdelhedi, R., and Savall, A. (2008). Improvement of the electrocatalytic activity of platinum in oxidation of aromatic compounds. Comptes Rendus Chim. *11*, 1254–1261. https://doi.org/10.1016/j.crci.2008.01.003.

Sandbeck, D.J.S., Secher, N.M., Speck, F.D., Sørensen, J.E., Kibsgaard, J., Chorkendorff, I., and Cherevko, S. (2020). Particle size effect on platinum dissolution: considerations for accelerated stability testing of fuel cell catalysts. ACS Catal. *10*, 6281–6290. https://doi.org/10.1021/acscatal.0c00779.

Shen, L.L., Zhang, G.R., Miao, S., Liu, J., and Xu, B.-Q. (2016). Core–Shell nanostructured Au@Ni$_m$Pt$_2$ electrocatalysts with enhanced activity and durability for oxygen reduction reaction. ACS Catal. *6*, 1680–1690. https://doi.org/10.1021/acscatal.5b02124.

Shinozaki, K., Zack, J.W., Pylypenko, S., Pivovar, B.S., and Kocha, S.S. (2015a). Oxygen reduction reaction measurements on platinum electrocatalysts utilizing rotating disk electrode technique. J. Electrochem. Soc. *162*, F1384–F1396. https://doi.org/10.1149/2.0551512jes.

Shinozaki, K., Zack, J.W., Richards, R.M., Pivovar, B.S., and Kocha, S.S. (2015b). Oxygen reduction reaction measurements on platinum electrocatalysts utilizing rotating disk electrode technique. J. Electrochem. Soc. 162, F1144–F1158. https://doi.org/10.1149/2.1071509jes.

Stamenkovic, V.R., Fowler, B., Mun, B.S., Wang, G., Ross, P.N., Lucas, C.A., and Marković, N.M. (2007). Improved oxygen reduction activity on Pt₃Ni(111) via increased surface site availability. Science 315, 493–497. https://doi.org/10.1126/science.1135941.

The Japan METI. (2018). Strategic Energy Plan. https://www.enecho.meti.go.jp/en/category/others/basic_plan/5th/pdf/strategic_energy_plan.pdf.

The State Council of China. (2021). The Outline of China's 14th Five-Year Plan (2021-2025). http://www.gov.cn/zhengce/content/2016-12/19/content_5150090.htm.

The US Department of Energy (DOE) (2016). Multi-year research, development, and demonstration plan: Fuel cells section. http://www.eere.energy.gov/hydrogenandfuelcells/mypp/pdfs/fuel_cells.pdf.

Tian, X.L., Zhao, X., Su, Y.Q., Wang, L.J., Wang, H.M., Dang, D., Chi, B., Liu, H.F., Hensen, E.J.M., Lou, X.W.D., and Xia, B.Y. (2019). Engineering bunched Pt–Ni alloy nanocages for efficient oxygen reduction in practical fuel cells. Science 366, 850–856. https://doi.org/10.1126/science.aaw7493.

Vidal-Iglesias, F.J., Arán-Ais, R.M., Solla-Gullón, J., Herrero, E., and Feliu, J.M. (2012). Electrochemical characterization of shape-controlled Pt nanoparticles in different supporting electrolytes. ACS Catal. 2, 901–910. https://doi.org/10.1021/cs200681x.

Viswanathan, V., Hansen, H.A., Rossmeisl, J., and Nørskov, J.K. (2012). Universality in oxygen reduction electrocatalysis on metal surfaces. ACS Catal. 2, 1654–1660. https://doi.org/10.1021/cs300227s.

Wan, K., Yu, Z.P., Li, X.P., Liu, M.Y., Yang, G., Piao, J.H., and Liang, Z.X. (2015). pH effect on electrochemistry of nitrogen-doped carbon catalyst for oxygen reduction reaction. ACS Catal. 5, 4325–4332. https://doi.org/10.1021/acscatal.5b01089.

Wan, X., Liu, X., Li, Y., Yu, R., Zheng, L., Yan, W., Wang, H., Xu, M., and Shui, J. (2019). Fe–N–C

electrocatalyst with dense active sites and efficient mass transport for high-performance proton exchange membrane fuel cells. Nat. Catal. 2, 259–268. https://doi.org/10.1038/s41929-019-0237-3.

Wang, D.L., Xin, H.L.L., Hovden, R., Wang, H.S., Yu, Y.C., Muller, D.A., DiSalvo, F.J., and Abruña, H.D. (2013). Structurally ordered intermetallic platinum–cobalt core–shell nanoparticles with enhanced activity and stability as oxygen reduction electrocatalysts. Nat. Mater. 12, 81–87. https://doi.org/10.1038/nmat3458.

Wang, X.X., Hwang, S.Y., Pan, Y.T., Chen, K., He, Y.H., Karakalos, S., Zhang, H.G., Spendelow, J.S., Su, D., and Wu, G. (2018). Ordered Pt₃Co intermetallic nanoparticles derived from metal-organic frameworks for oxygen reduction. Nano Lett. 18, 4163–4171. https://doi.org/10.1021/acs.nanolett.8b00978.

Wang, X.X., Sokolowski, J., Liu, H., and Wu, G. (2020a). Pt alloy oxygen-reduction electrocatalysts: synthesis, structure, and property. Chin. J. Catal. 41, 739–755. https://doi.org/10.1016/s1872-2067(19)63407-8.

Wang, X.X., Swihart, M.T., and Wu, G. (2019a). Achievements, challenges and perspectives on cathode catalysts in proton exchange membrane fuel cells for transportation. Nat. Catal. 2, 578–589. https://doi.org/10.1038/s41929-019-0304-9.

Wang, Y., Ruiz Diaz, D.F., Chen, K.S., Wang, Z., and Adroher, X.C. (2020b). Materials, technological status, and fundamentals of PEM fuel cells – a review. Mater. Today 32, 178–203. https://doi.org/10.1016/j.mattod.2019.06.005.

Wang, Y., Sun, D., Chowdhury, T., Wagner, J.S., Kempa, T.J., and Hall, A.S. (2019b). Rapid room-temperature synthesis of a metastable ordered intermetallic electrocatalyst. J. Am. Chem. Soc. 141, 2342–2347. https://doi.org/10.1021/jacs.8b09919.

Wang, Y.H., Le, J.B., Li, W.Q., Wei, J., Radjenovic, P.M., Zhang, H., Zhou, X.S., Cheng, J., Tian, Z.Q., and Li, J.F. (2019c). In situ spectroscopic insight into the origin of the enhanced performance of bimetallic nanocatalysts towards the oxygen reduction reaction (ORR). Angew. Chem. Int. Ed. 58, 16062–16066. https://doi.org/10.1002/anie.201908907.

WikiPedia (2021). Standard Hydrogen Electrode. https://en.wikipedia.org/wiki/Standard_hydrogen_electrode.

Xie, C., Niu, Z., Kim, D., Li, M., and Yang, P. (2020). Surface and interface control in nanoparticle catalysis. Chem. Rev. 120, 1184–1249. https://doi.org/10.1021/acs.chemrev.9b00220.

Xiong, Y., Yang, Y., DiSalvo, F.J., and Abruna, H.D. (2020). Synergistic bimetallic metallic organic framework-derived Pt–Co oxygen reduction electrocatalysts. ACS Nano 14, 13069–13080. https://doi.org/10.1021/acsnano.0c04559.

Xu, H., Shang, H., Wang, C., and Du, Y. (2020). Ultrafine Pt-based nanowires for advanced catalysis. Adv. Funct. Mater. 30, 2000793–2000810. https://doi.org/10.1002/adfm.202000793.

Yan, D., Li, H., Chen, C., Zou, Y., and Wang, S. (2019). Defect engineering strategies for nitrogen reduction reactions under ambient conditions. Small Methods 3, 1800331–1800351. https://doi.org/10.1002/smtd.201800331.

Zalitis, C.M., Kramer, D., and Kucernak, A.R. (2013). Electrocatalytic performance of fuel cell reactions at low catalyst loading and high mass transport. Phys. Chem. Chem. Phys. 15, 4329–4340. https://doi.org/10.1039/c3cp44431g.

Zhang, B., Fu, G., Li, Y., Liang, L., Grundish, N.S., Tang, Y., Goodenough, J.B., and Cui, Z. (2020a). General strategy for synthesis of ordered Pt₃M intermetallics with ultrasmall particle size. Angew. Chem. Int. Ed. Engl. 59, 7857–7863. https://doi.org/10.1002/anie.201916260.

Zhang, X., Wang, Y., Gu, M., Wang, M., Zhang, Z., Pan, W., Jiang, Z., Zheng, H., Lucero, M., Wang, H., et al. (2020b). Molecular engineering of dispersed nickel phthalocyanines on carbon nanotubes for selective CO₂ reduction. Nat. Energy 5, 684–692. https://doi.org/10.1038/s41560-020-0667-9.

Zhao, Y., Bai, J., Wu, X.-R., Chen, P., Jin, P.-J., Yao, H.-C., and Chen, Y. (2019). Atomically ultrathin RhCo alloy nanosheet aggregates for efficient water electrolysis in broad pH range. J. Mater. Chem. A 7, 16437–16446. https://doi.org/10.1039/c9ta05334d.

Zhu, Z., Liu, Q., Liu, X., and Shui, J. (2020). Temperature impacts on oxygen reduction reaction measured by the rotating disk electrode technique. J. Phys. Chem. C 124, 3069–3079. https://doi.org/10.1021/acs.jpcc.9b10173.

STAR★METHODS

KEY RESOURCES TABLE

REAGENT or RESOURCE	SOURCE	IDENTIFIER
Chemicals, peptides, and recombinant proteins		
Commercial 20%Pt/C	Johnson Matthey Fuel Cells	Cat#S128513
Perchloric acid (71 wt.%)	Tianjin Zhengcheng	CAS: 7601-90-3
Nafion Solution (5%)	Macklin	CAS: 31175-20-9
2-methlimidazole	Shanghai Aladdin	CAS: 693-98-1
$Zn(NO_3)_2 \cdot 6H_2O$	Shanghai Aladdin	CAS: 10196-18-6
$Fe(NO_3)_3 \cdot 9H_2O$	Shanghai Aladdin	CAS: 7782-61-8
Methanol Anhydrous	Tianjin Tianli	CSA: 170082-17-4
Ethanol Absolute	SinoPharm	CSA: 64-17-5
Deionized Water (18.25 mΩ)	Chengdu Youyue	CSA: 7732-18-5
Software and algorithms		
Origin 2016	Graphing and data analysis software from OriginLab	https://www.originlab.com/
Office 2016	Microsoft	https://www.microsoft.com/
Other		
Pine Research MSR Rotator	Pine Research	https://www.pineresearch.com/
Bruker D8 diffractometer	Bruker Corporation	https://www.bruker.com/
JEM-F200	JEOL	https://www.jeol.co.jp

RESOURCE AVAILABILITY

Lead contact

Further information and requests for resources should be directed to and will be fulfilled by the lead contact, Zhen-Bo Wang (wangzhb@hit.edu.cn).

Materials availability

This study did not generate new materials.

Data and code availability

All data supporting this study are available in the manuscript and supplemental information.

METHOD DETAILS

Preparation of reversible hydrogen electrode (RHE)

Perchloric acid ($HClO_4$, 71 wt.%) was diluted to aqueous solutions of 3 mol/L, 1 mol/L, 0.3 mol/L, and 0.1 mol/L with DI-water (18.25 mΩ), whose tested pH values are (-0.48), 0.12, 0.58, and 1.06 (Table S1), respectively. Then the prepared solution was injected into a semi-closed cavity of quartz capillary of RHE carefully, followed by a transfer to a beaker with the same $HClO_4$ solution acting as the electrolyte. Then an electrolysis was performed with RHE acting as the anode and Pt mesh electrode acting as the cathode and reference electrode (RE). The potential of RHE was set at -4–-5 V vs. Pt mesh electrode to produce a coherent H_2 cylinder inside the RHE quartz capillary (Figure S1). The RHE electrode should stand at least 30 mins to get a stable potential before it could be used as an RHE. In fact, two RHEs were made for each electrolyte of different pH and those two RHEs are calibrated with each other to ensure their reliability.

Calibration of REs with respect to RHE

Two all-new and two stale mercury-mercurous sulfate electrodes (MSEs) were calibrated in $HClO_4$ electrolytes of different pH, and the specific operation is shown in Figure 5A in the main text. The thermodynamic

potential of all-new MSE provided by the manufacturer (Tianjin Aida Hengsheng, China) is 652 mV vs. normal hydrogen electrode (NHE).

Synthesis of Fe-N-C PGM-free catalyst

3.39 g $Zn(NO_3)_2 \cdot 6H_2O$ and 0.10 g $Fe(NO_3)_3 \cdot 9H_2O$ were dissolved in a conical flask containing 300 mL anhydrous methanol (A solution). 3.94 g 2-methlimidizole was dissolved in a round-bottom flask containing 300 mL anhydrous methanol (B solution). A solution was poured into B solution under vigorous stirring, and the mixed solution was kept at ambient temperature for 20 mins before it was transferred into a thermostat setting at 60 °C. After ~24 hours, the precipitation was centrifuged and washed with ethanol three times, then the product was dried in a vacuum oven setting at 60 °C overnight. The light yellow material (Fe doped ZIF-8) was ground and then transferred into a furnace with Argon (Ar) protection, followed by a 1050 °C carbonization process for 90 mins. The black powder is marked as Fe-N-C PGM-free catalyst.

Material characterization

The crystal structures were identified by powder X-ray diffraction (XRD) on a Bruker D8 diffractometer with Cu $K_{\alpha 1}$ X-rays (λ=1.5406 Å). The morphologies and microstructures were observed by a field emission TEM (JEM-F200, 200 kV), equipped with an Oxford EDX detector and a Gatan EELS spectrometer.

The preparation of working electrode (WE)

5 mg of catalyst (Commercial 20% Pt/C or Fe-N-C PGM-free catalyst) was dispensed in a mixed solution (500 μL DI-water + 500 μL ethanol + 30 μL 5% Nafion solution) followed by a 40 mins sonication. The obtained ink was drop-casted on the surface of a pre-polished glassy-carbon electrode (RRDE) and dried under an infrared light for 20 mins to act as a WE. The tests were performed in an electrochemical cell as demonstrated in Figure 1, and Pt mesh and RHE were used as counter electrode (CE) and RE, respectively. The PGM loading is 40.6 $\mu g_{Pt}/cm^2$ for 20% Pt/C; the total loading is 609 $\mu g/cm^2$ for Fe-N-C PGM-free catalyst.

The Linear sweep voltammetry (LSV) for ORR

The 20%Pt/C WE was activated in Ar saturated 0.1 M $HClO_4$ electrolyte via a cyclic voltammetry test (CV, Ar, 0.05–1.05 V, 100 mV/s, 25 cycles), then an Ar CV test (Ar, 0.05–1.05 V, 50 mV/s, 6 cycles) was performed in the same cell. After that, WE needed to be subjected to an Ar LSV (Ar, Quiet time 60 s, 1.05–0.05 V, 10 mV/s, Sample interval 0.1 mV, 1600 rpm) test beforehand. Then the WE was transferred to another cell with O_2 saturated 0.1 M $HClO_4$, and O_2 activation and O_2 CV were adopted in sequence to make sure the stability of WE. After that, LSV (O_2, Quiet time 60 s, 1.05–0.05 V, 10 mV/s, Sample interval 0.1 mV, 1600 rpm) was performed on the WE, and the potential of ring electrode was fixed at 1.20 V. LSVs were performed negatively (negative-going, from 1.05 V to 0.05 V) and positively (positive-going, from 0.05 V to 1.05 V). To ensure the reliability of the test results, two electrodes were used for each test. All tests in this work were performed at ~25 °C.

The staircase voltammetry (SCV) for ORR

The WE underwent the same Ar activation, Ar CV, O_2 activation and O_2 CV processes as in LSV test. After that, SCV (O_2, Quiet time 60 s, 1.05–0.05 V, Incre E 50 mV, Step period 30 s, 1600 rpm) were performed on the WE, and the potential of ring electrode was fixed at 1.20 V. SCVs were performed negatively (negative-going, from 1.05 V to 0.05 V) and positively (positive-going, from 0.05 V to 1.05 V) for both 20%Pt/C and Fe-N-C PGM-free catalysts.

The hydrogen peroxide yield (H_2O_2%) calculation

The hydrogen peroxide yield was calculated with the following equation.

$$H_2O_2\% = \frac{200 \cdot J_r}{J_r + N \cdot J_d}\%$$

J_r: the ring current or current density (mA or mA/cm^2), J_d: the disk current or current density (mA or mA/cm^2), N: collection coefficient of the RRDE instrument (here is 37%).